# Deformation of a free interface pierced by a tilted cylinder: variation of the contact angle

Christophe Raufaste[a,*], Simon Cox[b]

[a]Laboratoire de Physique de la Matière Condensée, CNRS UMR 7336, Université de Nice Sophia-Antipolis, 06108 Nice, France
[b]Institute of Mathematics and Physics, Aberystwyth University, Aberystwyth SY23 3BZ, UK

**Abstract**

We investigate the effects of the contact angle $\theta_w$, and the angle of inclination $\theta_i$ on the interaction between an infinite cylinder and a free fluid-fluid interface governed only by its surface tension. We describe a numerical method to calculate the deformation of the interface, and use it to validate a theory for the force on the cylinder based only on knowledge of the interface shape where it meets the cylinder.

*Keywords:* interface, surface tension, cylinder, energy minimization

## 1. Introduction

There are many instances of a long slender object piercing an interface such as a liquid surface or a soap film. They appear in applications throughout biology and engineering, and include animal locomotion [1, 2, 3, 4]; surface processing for nano-micro-applications, for example fiber coating and cleaning [5, 6, 7], the assembly of hairs, carbon nanotubes and biological filaments [8, 9, 10, 11, 12, 13, 14, 15, 16]; uses of AFM probes [6, 17, 18]; and impact of liquid jets [19].

There are a number of methods for calculating the interface shape by integrating the Young-Laplace equation with given boundary conditions. These include mesh-free finite difference methods [20]; boundary-element simulations [21]; Surface Evolver simulations coupled to finite-difference simulations [22]; and an ordinary differential equation solver (MATLAB) [3].

In previous work [23], we showed that in the case of total wetting ($\theta_w = 0$), the force on the cylinder is vertical, irrespective of the angle of inclination $\theta_i$, and its magnitude (which does depend on the inclination) can be calculated from the shape of the contact line according to

$$F_z = 2\gamma\pi R/\cos(\theta_i), \tag{1}$$

where $\gamma$ is the surface tension of the interface and $R$ is the radius of the cylinder. This result agrees with Neukirch's energetic approach to describing the geometry of an infinite soap film totally wetting a strip [10].

Here, we show how to generalise the approach to non-zero contact angles. A simple expression is proposed to quantify the contact line distortion as a function of the inclination angle.

## 2. Simulations

We use the Surface Evolver [24] to calculate the shape of a single area-minimizing surface that meets a cylindrical rod, inclined at an angle $\theta_i$ to the vertical, at a contact angle of $\theta_w$. The Surface Evolver works by refining the surface into a mesh of many small triangles, and moving the vertices of these triangles so as to minimize the energy of the interface-cylinder system. This method was previously validated in the case $\theta_w \approx 0$ [23], and indeed this is the most severe test of the numerics. All units are dimensionless, without loss of generality.

We first create a planar surface in the O$xy$ plane in a fixed square frame of side-length 5.0 and a cylinder, with axis in the vertical ($z$) direction and radius $R = 0.1$, through its centre. The tension of the surface is $\cos(\theta_w)^{-1}$ and, to ensure that the cylinder is partially wetted, we include a virtual liquid film on the lower half of the cylinder with unit tension. We use the highest level of refinement described in [23], with roughly 14,000 triangles, and 81 vertices around the contact line. This proves insufficient only when $\theta_w$ is less than about 10° *and* $\theta_i$ is larger than about 65°, for which a higher level of refinement around the cylinder is required. (This is more significant in determining the accuracy than increasing the size of the square frame.)

One iteration consists of tilting the cylinder by $\Delta\theta_i = 1.5°$ in the $x - z$ plane and finding the new minimum area configuration of the surface (Fig. 1). Convergence requires up to 6000 conjugate gradient iterations, which takes about one hour on a desktop PC. At each iteration, the location of the points along the contact line is recorded

*Corresponding author. Tel.: +33 4 92 07 63 18 ; Fax: +33 4 92 07 67 54.
*Email address:* Christophe.Raufaste@unice.fr (Christophe Raufaste)

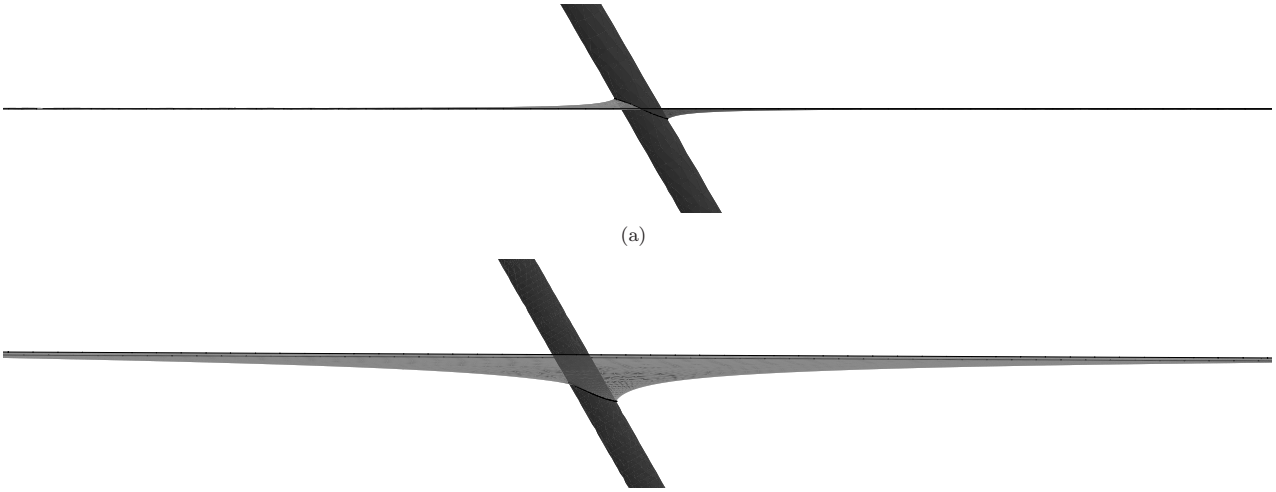

(a) (b)

Figure 1: Side view of a simulation, showing how the interface deforms, in the case $\theta_i = 30°$, with an imposed contact angle of (a) $\theta_w = 90°$ and (b) $\theta_w = 60°$.

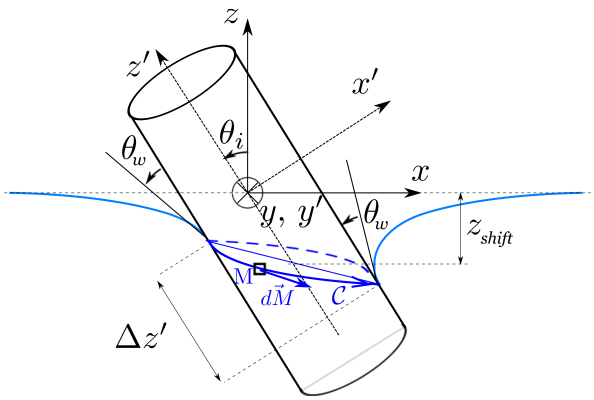


Figure 2: Schematic representation of the interface-cylinder system.

which, as we shall show below, is sufficient to calculate all quantities of interest.

The shape and position of the contact line where the interface meets the cylinder is sketched in Fig. 2. To describe our results we will denote the reference frame of the initially flat interface as $\mathcal{R}$ (O$xyz$), with O$x$ horizontal, and the reference frame of the cylinder as $\mathcal{R}'$ (O$x'y'z'$); they are related by

$$\begin{aligned} x' &= \cos(\theta_i)x + \sin(\theta_i)z, && \text{(2a)} \\ y' &= y, && \text{(2b)} \\ z' &= -\sin(\theta_i)x + \cos(\theta_i)z. && \text{(2c)} \end{aligned}$$

In the reference frame of the cylinder, $\mathcal{R}'$, with cylindrical coordinates ($r'$, $\theta'$, $z'$), any point $M$ has $\vec{OM} = x'\vec{e}_{x'} + y'\vec{e}_{y'} + z'\vec{e}_{z'} = r'\vec{e}_{r'} + \theta'\vec{e}_{\theta'} + z'\vec{e}_{z'}$, with

$$\begin{aligned} x' &= r'\cos(\theta') && \text{(3a)} \\ y' &= r'\sin(\theta') && \text{(3b)} \\ \vec{e}_{r'} &= \cos(\theta')\vec{e}_{x'} + \sin(\theta')\vec{e}_{y'} && \text{(3c)} \\ \vec{e}_{\theta'} &= -\sin(\theta')\vec{e}_{x'} + \cos(\theta')\vec{e}_{y'}. && \text{(3d)} \end{aligned}$$

By symmetry, the contact line is given by

$$\begin{aligned} r' &= R && \text{(4a)} \\ z' &= z'(\theta'), && \text{(4b)} \end{aligned}$$

with $\theta' \in [-\pi, \pi]$.

| contact angle $\theta_w$ | 2° | 15° | 30° | 45° | 60° | 75° | 90° |
|---|---|---|---|---|---|---|---|
| symbol | ○ | □ | ◇ | ∗ | ▷ | ◁ | ▽ |

Table 1: The key used to represent different contact angles in the figures.

## 3. Results

### *3.1. Distortion and shift of the contact line*

The shape and position of the contact line, referred to the reference frame of the cylinder $\mathcal{R}'$, for different $\theta_i$ and $\theta_w$, are shown in Figs. 3 and 4. Observe that the contact line is stretched, distorted, and shifted as $\theta_i$ and $\theta_w$ vary.

The *distortion* of the contact line is defined by the difference in its height on two sides of the cylinder:

$$\Delta z' = z'_{\theta'=\pi} - z'_{\theta'=0}. \qquad (5)$$

The (dimensionless) relative perimeter of the contact line $\mathcal{P}/2\pi R - 1$ is also used to quantify its deformation.

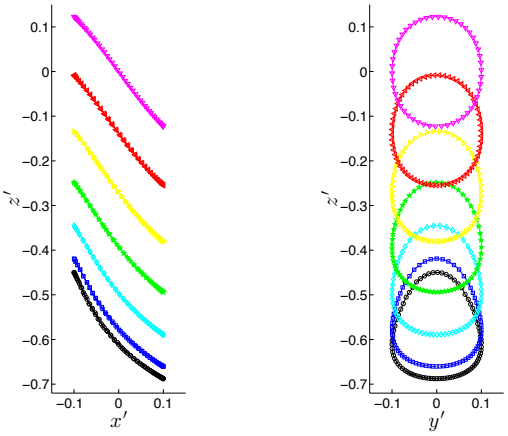


(a) (b)

Figure 3: Projection of the contact line on to (a) the O$x'z'$ plane and (b) the O$y'z'$ plane in the reference frame of the cylinder $\mathcal{R}'$ for $\theta_i = 30°$. The contact angle $\theta_w$ increases upwards, according to the key in Table 1.

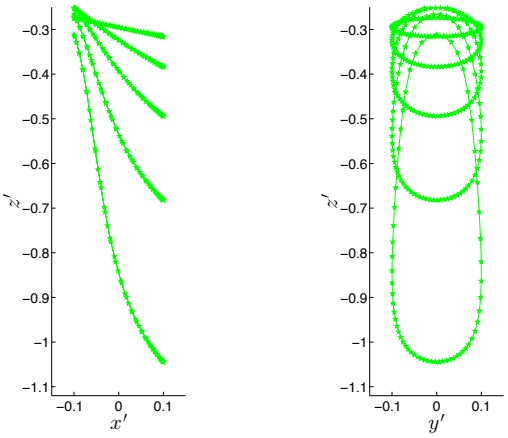


(a) (b)

Figure 4: Projection of the contact line on to (a) the O$x'z'$ plane and (b) the O$y'z'$ plane in the reference frame of the cylinder $\mathcal{R}'$ for $\theta_w = 45°$. From top to bottom $\theta_i = 6°$, 18°, 30°, 42° and 54°.

If $\mathcal{A}_{x'y'}$, $\mathcal{A}_{x'z'}$ and $\mathcal{A}_{y'z'}$ denote the absolute values of the area enclosed by the contact line when projected on the (O$x'y'$), (O$x'z'$) and (O$y'z'$) planes respectively, then by symmetry, $\mathcal{A}_{x'y'} = \pi R^2$ and $\mathcal{A}_{x'z'} = 0$. For a given $\theta_w$, $\mathcal{A}_{y'z'}$ and $\Delta z'$ are equal to zero when $\theta_i = 0$ and both increase monotonically as $\theta_i$ increases. Fig. 5 shows how the perimeter of the contact line and its distortion $\Delta z'/R$ depend on $\theta_i$ and $\theta_w$. In particular, note that the effect of $\theta_w$ is weak in each case.

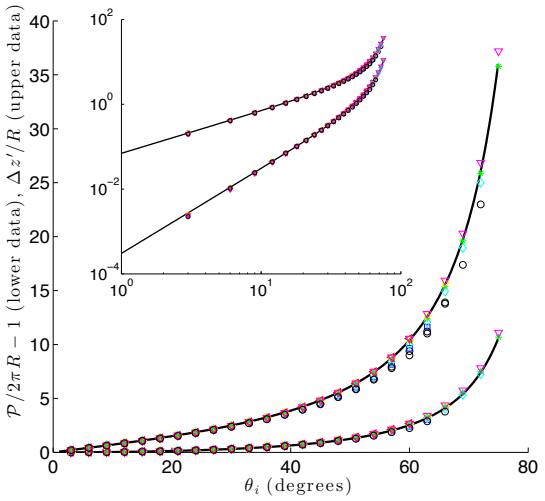


Figure 5: The relative perimeter (lower data) and distortion (Eq. (5)) (upper data) plotted versus the inclination angle. Solid lines are for the model described in § 4.1. Insert: same data plotted on log axes, showing that the agreement is good even at small angles.

### *3.2. Force measurement*

Following the approach for $\theta_w = 0$ [23], we generalize the force measurement to any value of $\theta_w$.

We denote by M($R$, $\theta'$, $z'(\theta')$) a point on the contact line and $d\vec{M}$ an infinitesimal variation of position along the contact line (Fig. 2):

$$d\vec{M} = Rd\theta'\vec{e}_{\theta'} + dz'\vec{e}_{z'} = d\theta'\left(R\vec{e}_{\theta'} + \frac{dz'}{d\theta'}\vec{e}_{z'}\right).$$

For total wetting ($\theta_w = 0$), the local force $d\vec{F}|_{\theta_w=0}$ on $d\vec{M}$ is perpendicular to $d\vec{M}$ and to $\vec{e}_{r'}$:

$$d\vec{F}|_{\theta_w=0} = \gamma\vec{e}_{r'} \wedge d\vec{M}. \qquad (6)$$

This generalizes to any contact angle $\theta_w$ as follows:

$$d\vec{F} = \gamma\cos(\theta_w)\vec{e}_{r'} \wedge d\vec{M} + \gamma\sin(\theta_w)\vec{e}_{r'}ds,$$

with $ds = \|d\vec{M}\|$ the infinitesimal arclength along the contact line, which gives

$$\vec{F} = \gamma\cos(\theta_w)\oint_{\mathcal{C}}\vec{e}_{r'} \wedge d\vec{M} + \gamma\sin(\theta_w)\oint_{\mathcal{C}}\vec{e}_{r'}ds. \qquad (7)$$

The first integral was shown in [23] to be equal to

$$\oint_{\mathcal{C}} \vec{e}_{r'} \wedge d\vec{M} = \frac{\mathcal{A}_{y'z'}}{R}\vec{e}_{x'} + 2\pi R\vec{e}_{z'}.$$

The second can be expanded using

$$\begin{aligned}\oint_{\mathcal{C}} \vec{e}_{r'} ds &= \oint_{\mathcal{C}} \cos(\theta')\vec{e}_{x'} + \sin(\theta')\vec{e}_{y'} ds \\ &= \oint_{\mathcal{C}} \cos(\theta') ds\vec{e}_{x'} + \oint_{\mathcal{C}} \sin(\theta') ds\vec{e}_{y'} \\ &= \frac{1}{R}\oint_{\mathcal{C}} x' ds\vec{e}_{x'} + \frac{1}{R}\oint_{\mathcal{C}} y' ds\vec{e}_{y'} \\ &= \frac{1}{R}\oint_{\mathcal{C}} x' ds\vec{e}_{x'}.\end{aligned}$$

This gives the expression for the force on the cylinder in the reference frame $\mathcal{R}'$:

$$\begin{aligned}F_{x'} &= 2\gamma\pi R\left(\cos(\theta_w)\frac{\mathcal{A}_{y'z'}}{2\pi R^2} + \sin(\theta_w)\frac{1}{2\pi R^2}\oint_{\mathcal{C}} x' ds\right) \\ F_{y'} &= 0 \\ F_{z'} &= 2\gamma\pi R\cos(\theta_w),\end{aligned}$$

which is related to the force in the reference frame $\mathcal{R}$ by

$$F_x = \cos(\theta_i)F_{x'} - \sin(\theta_i)F_{z'}, \quad (8a)$$
$$F_y = 0, \quad (8b)$$
$$F_z = \sin(\theta_i)F_{x'} + \cos(\theta_i)F_{z'}. \quad (8c)$$

We observe in our simulations that the force is always vertical in the reference frame $\mathcal{R}$ (data not shown). Introducing the condition $F_x = 0$ in our force expressions (Eq. (8)) leads, after some manipulation, to the following prediction for the vertical force:

$$F_z/2\gamma\pi R = \cos(\theta_w)/\cos(\theta_i), \quad (9)$$

which is validated in Fig. 6 by plotting $F_z$ for all values of $\cos(\theta_w)$ and $\cos(\theta_i)$.

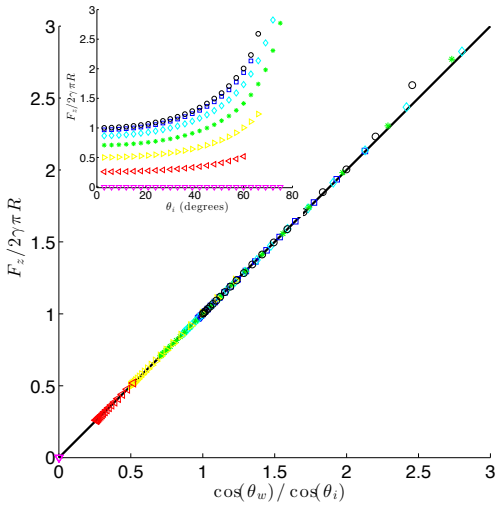


Figure 6: Force measurements. The dimensionless vertical force $F_z/2\pi R$ versus $\cos(\theta_w)/\cos(\theta_i)$. One point is slightly off the linear main trend, indicating a lack of mesh refinement when $\theta_w \lesssim 10°$ and $\theta_i \gtrsim 65°$ (see § 2). Insert: the dimensionless vertical force vs the inclination angle for all data points.

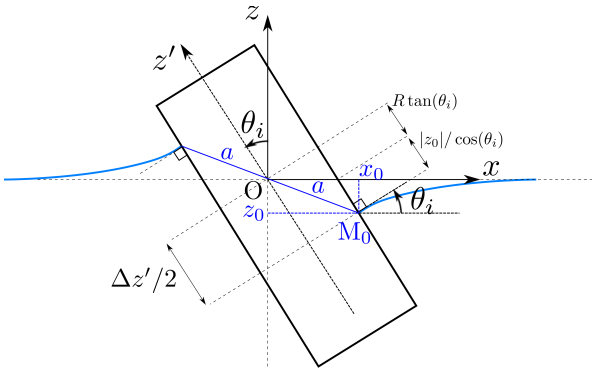


Figure 7: 2D projection of the film shape for $\theta_w = 90°$ showing the various geometrical quantities defined in the text.

## 4. Discussion

The cylinder perturbs the soap film, and this perturbation relaxes towards the horizontal as the distance from the cylinder increases. Although a description of the exact film shape is highly non-trivial [25], it is possible to characterize the film shape and distortion using approximations. We also give an empirical expression for the distortion of the contact line $\Delta z'$.

### *4.1. Film shape*

The film shape can be described in terms of its height above the underformed film in cylindrical coordinates, $z = S(r,\theta)$. This is shown in Fig. 8 for several $\theta_i$ in the case $\theta_w = 90°$.

Assuming that the film is a minimal surface, the mean curvature is equal to zero. If we make the convenient and often-used assumption that the gradient of $S$ is small, then $S(r,\theta)$ satisfies Laplace's equation, and a separable solution of the form

$$S(r,\theta) = \sum_{n=1}^{\infty} A_n \frac{\cos((2n-1)\theta)}{r^{2n-1}} \quad (10)$$

is appropriate for the case $\theta_w = 90°$ (which is the case with the highest degree of symmetry; other terms would be needed for other $\theta_w$). For that wetting angle, our results indicate (data not shown) that the fundamental mode is dominant whatever the inclination angle, but that the higher order terms gain in importance close to the cylinder as $\theta_i$ increases. In particular, we find that the fundamental

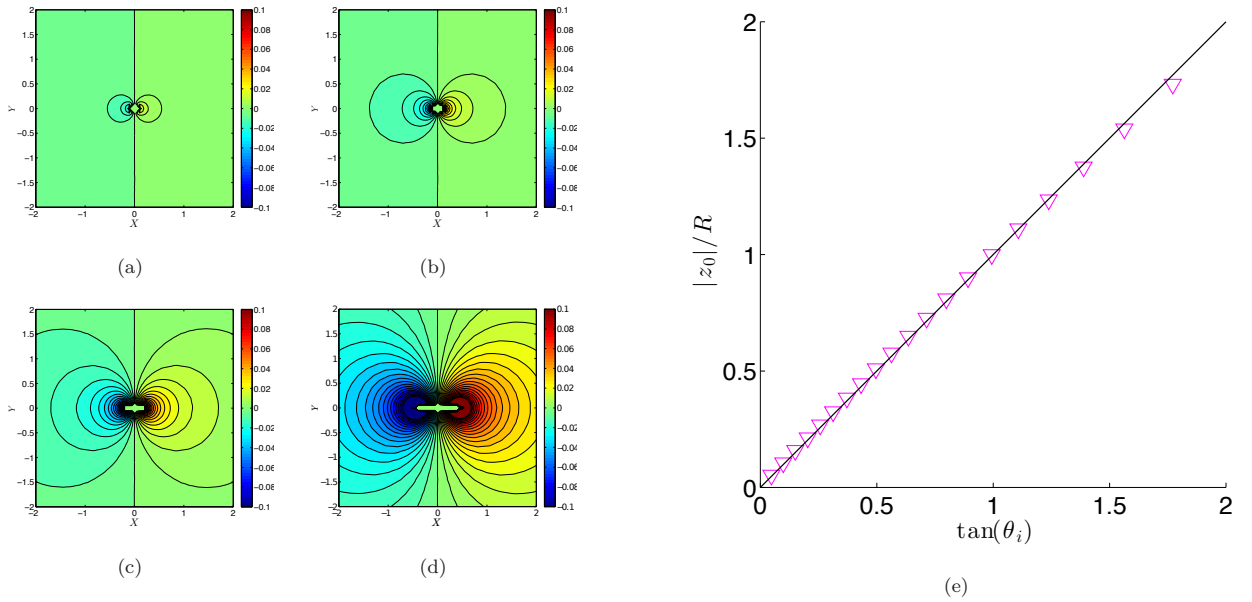


Figure 8: Film characterization for $\theta_w = 90°$. Contour plot of film height $S$ for (a) $\theta_i = 15°$, (b) 30°, (c) 45° and (d) 60°. (e) $|z_0|/R$ versus $\tan(\theta_i)$ for all inclination angles.

mode is sufficient to describe the distortion of the contact line for small $\theta_i$, but fails for larger inclination angles.

### *4.2. Empirical approach*

We denote by $\mathrm{M}_0(x_0, z_0)$ the point at which the film touches the cylinder in the $Oxz$ plane (Fig. 7). For $\theta_w = 90°$, we find empirically that the position of $\mathrm{M}_0$, as a function of the inclination angle, is well approximated by the following expression (Fig. 8e):

$$z_0 \simeq -R\tan(\theta_i). \tag{11}$$

From geometrical considerations (Fig. 7), the distortion can then be expressed as

$$\Delta z' = 2(R\tan(\theta_i) + |z_0|/\cos(\theta_i))$$

which leads to the following empirical expression for the contact line distortion:

$$\Delta z' \simeq 2R\tan(\theta_i)\left(1 + \frac{1}{\cos(\theta_i)}\right). \tag{12}$$

It is remarkable that this expression shows excellent agreement with measurements for all $\theta_i$ and all $\theta_w$ (Fig. 5) and that such a simple law (Eq. 11) captures the effect of the whole contact line, despite the fact that this profile is determined by a local condition (that the contact angle is equal to $\theta_w$). Eq. (12) should be useful in testing models or possible candidates to describe the whole film shape.

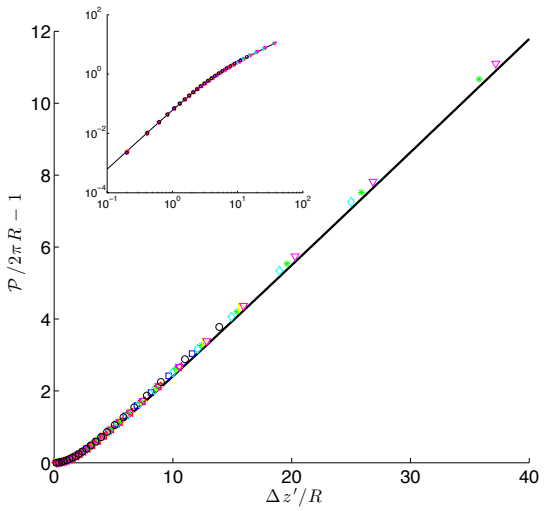


Figure 9: Ellipse approximation. The dimensionless relative perimeter versus the dimensionless distortion. The solid line holds for the ellipse approximation model described in the main text. Insert: same data plotted on log axes, showing that the agreement is good even at very small $\Delta z'/R$.

### *4.3. Contact line profile - elliptical approximation*

Plots of the contact line profiles (Figs. 3 and 4) suggest that they are roughly elliptical. This approximation certainly appears appropriate for the smallest $\theta_i$ and the

largest $\theta_w$. Approximating the contact line as an ellipse allows us to link $\Delta z'$ and $\mathcal{P}$. The ellipse should have a semi-major axis $a = R\sqrt{1 + \frac{1}{4}\left(\frac{\Delta z'}{R}\right)^2}$ (see Fig. 7) in the $Oxz$ plane and a semi-minor axis $b = R$ in the perpendicular direction. The ellipse perimeter can be estimated using Ramanujan's approximation:

$$\mathcal{P} = \pi\left(3(a+b) - \sqrt{(3a+b)(3b+a)}\right),$$

and compared with simulations by plotting $\mathcal{P}/2\pi R - 1$ versus $\Delta z'/R$, as shown on Fig. 9. The comparison is satisfactory even at large $\theta_i$ and small $\theta_w$, validating its use.

Combining this with the empirical expression for the film shape (§4.2) as a way to predict the distortion $\Delta z'$, we can directly compare perimeter measurements with this model on Fig. 5. Again, good agreement is found.

## 5. Conclusions

We have studied the deformation of a free interface pierced by a tilted cylinder, varying both the contact angle and the angle of inclination of the cylinder. We derive equations that link the position of the contact line to the interaction force, and give an explicit expression for the latter (Eq. (9)).

The deformation of the interface may be characterized by a superposition of cylindrical harmonics, the first of which is dominant and sufficient to describe the far field perturbation. We give an empirical expression for the distortion of the contact line (Eq. (12)) valid for all inclinations and contact angles.

In terms of the applications cited in the introduction, it is clear how our expression for the interaction force, for any contact angle and inclination angle, is of significance in interpreting data from AFMs, for example. Further, we have shown that the contact angle does not play a significant role in the distortion and perimeter of the contact line, and that there is an unique relation between each of the latter quantities and the angle of inclination; these will be useful in determining optimal processing conditions in areas such as fiber coating. For a given inclination angle, the contact line is shifted downward as the contact angle decreases, since the smaller the contact angle, the larger the force, and consequently the larger the deformation of the interface; we expect this result to give insight into animal locomotion on the surface of a liquid.

In future work it will be interesting to change the shape of the object that pierces the interface [22, 21], and to characterize the interaction between several objects [20], again varying systematically both the contact angle and the angle of inclination. In principle, the method could be applied to a wide range of systems in which gravity does not play a role.

Further terms could be added to the energy of the system, for instance a line tension where the interface meets the cylinder, which would improve the accuracy of our method close to a wetting transition. This would allow an exploration of the effect of line tension on the shape that the interface takes, and thus the force that it exerts on the object (see e.g. [26]). As the size of the object tends to zero, we expect the line tension to become more important, until a regime is reached in which the wetting properties dominate [26].


## Acknowledgments

We thank Ken Brakke for providing and maintaining the Surface Evolver, and Franck Celestini and Geoffroy Kirstetter for fruitful discussions.


## References


[1] D. L. Hu, B. Chan and J. W. M. Bush, The hydrodynamics of water strider locomotion, *Nature* 424, 663–666 (2003).

[2] D. L. Hu and J. W. M. Bush, Meniscus-climbing insects, *Nature* 437, 733–736 (2005).

[3] D. Vella, Floating Objects with Finite Resistance to Bending, *Langmuir* 24, 8701–8706 (2008).

[4] Y. Su, B. Ji, Y. Huang and K.-c. Hwang, Nature's Design of Hierarchical Superhydrophobic Surfaces of a Water Strider for Low Adhesion and Low-Energy Dissipation, *Langmuir* 26, 18926–18937 (2010).

[5] E. Lorenceau, C. Clanet and D. Quéré, Capturing drops with a thin fiber, *J. Colloid Interface Sci.* 279, 192–197 (2004).

[6] B. J. Mullins, A. Pfrang, R. D. Braddock, T. Schimmel and G. Kasper, Detachment of liquid droplets from fibres-Experimental and theoretical evaluation of detachment force due to interfacial tension effects, *J. Colloid Interface Sci.* 312, 333–340 (2007).

[7] Z. Huang, X. Liao, Y. Kang, G. Yin and Y. Yao, Equilibrium of drops on inclined fibers, *J. Colloid Interface Sci.* 330, 399–403 (2009).

[8] A. E. Cohen and L. Mahadevan, Kinks, rings, and rackets in filamentous structures, *PNAS* 100, 12141–12146 (2003).

[9] N. Chakrapani, B. Wei, A. Carrillo, P. M. Ajayan and R. S. Kane, Capillarity-driven assembly of two-dimensional cellular carbon nanotube foams, *PNAS* 101, 4009–4012 (2004).

[10] S. Neukirch, B. Roman, B. de Gaudemaris, J. Bico, Piercing a liquid surface with an elastic rod: Buckling under capillary forces, *Journal of the Mechanics and Physics of Solids* 55, 1212–1235 (2007).

[11] K. J. Park and H.-Y. Kim, Bending of floating flexible legs, *J. Fluid Mech.* 610, 381–390 (2008).

[12] M. L. Blow and J. M. Yeomans, Superhydrophobicity on Hairy Surfaces, *Langmuir* 26, 16071–16083 (2010).

[13] F. Chiodi, B. Roman and J. Bico, Piercing an interface with a brush: Collaborative stiffening, *Europhysics Letters* 90, 44006 (2010).

[14] H. Duan, and K. K. Berggren, Directed Self-Assembly at the 10 nm Scale by Using Capillary Force-Induced Nanocohesion, *Nano Lett.* 10, 3710–3716 (2010).

[15] S. Tawfick, M. De Volder and A. J. Hart, Structurally Programmed Capillary Folding of Carbon Nanotube Assemblies, *Langmuir* 27, 6389–6394 (2011).

[16] J. Bico, B. Roman, L. Moulin, A. Boudaoud, Elastocapillary coalescence in wet hair, *Nature* 432, 690 (2004) .

[17] S. D. A. Connell, S. Allen, C. J . Roberts, J . Davies, M. C. Davies, S. J. B. Tendler and P. M. Williams, Investigating the interfacial properties of single-liquid nanodroplets by Atomic Force Microscopy, *Langmuir* 18, 1719–1728 (2002).

[18] X. Xiong, S. Guo, Z. Xu, P. Sheng and P. Tong, Development of an atomic-force-microscope-based hanging-fiber rheometer for interfacial microrheology, *Physical Review E* 80, 061604 (2009).

[19] G. Kirstetter, C. Raufaste and F. Celestini, Jet impact on a soap film, *Physical Review E* 86, 036303 (2012).
[20] H. Cooray, P. Cicuta and D. Vella, The capillary interaction between two vertical cylinders, *J. Phys.: Condens. Matter* 24, 284104 (2012).
[21] C. Pozrikidis, Capillary attraction of floating rods, *Eng. Anal. Boundary Elem.* 36, 836–844 (2012).
[22] M. Cavallaro, L. Botto, E. P. Lewandowski, M. Wang and K. J. Stebe, Curvature-driven capillary migration and assembly of rod-like particles, *PNAS* 108, 20923–20928 (2011).
[23] C. Raufaste, G. Kirstetter, F. Celestini and S. J. Cox, Deformation of a free interface pierced by a tilted cylinder, *Europhysics Letters* 99, 24001 (2012).
[24] K. Brakke, The Surface Evolver, *Exp. Math.* 1, 141–165 (1992).
[25] M.M. Nicolson, The Interaction between Floating Particles, *Proc. Camb. Phil. Soc. Math. Phys. Sci.* 45, 288–295 (1949).
[26] A. O. Parry and C. Rascón, Fluid adsorption at the base of a cylinder, *Phys. Rev. Lett.* 107, 206104 (2011).